Research Square

Preprints are preliminary reports that have not undergone peer review.
They should not be considered conclusive, used to inform clinical practice,
or referenced by the media as validated information.

Self-Intercalation Strategy for Enhanced Transport in All-MoX2 (X = S, Se) Lateral Heterostructures: A First-Principles Study

Huan Wang
Harbin Normal University
Xiaojie Liu
Harbin Normal University
Hui Wang
Harbin Normal University
Haitao Yin
wlyht@126.com

Harbin Normal University

Article

Keywords: Self-intercalation, MoX2, Transport, First principles

Posted Date: February 26th, 2026

DOI: https://doi.org/10.21203/rs.3.rs-8558325/v1

License: This work is licensed under a Creative Commons Attribution 4.0 International License.
Read Full License

Additional Declarations: No competing interests reported.

Self-Intercalation Strategy for Enhanced Transport in All-MoX_2 (X = S, Se) Lateral Heterostructures: A First-Principles Study

Huan Wang[1,2], Xiaojie Liu[1*], Hui Wang[1*], Haitao Yin[1*]

1. Key Laboratory for Photonic and Electronic Bandgap Materials of Ministry of Education, School of Physics and Electronic Engineering, Harbin Normal University, Harbin, 150025, China

2. College of Science, Qiqihar University, Qiqihar, 161006, China

Abstract: To address the challenge of developing post-Moore-era field-effect transistors, we propose a self-intercalation (si) strategy that converts semiconducting MoX_2 (X = S, Se) into a metallic si-MoX_2 phase, enabling the construction of all-MoX_2 lateral heterojunctions. Using first-principles calculations, we systematically investigate the electronic structure of si-MoX_2 and the transport properties of the resulting si-MoX_2/MoX_2 heterojunctions. The results indicate that band hybridization induced by the intercalated Mo atoms drives a semiconductor-to-metal transition. Among the lateral heterojunctions, si-MoS_2/MoS_2 exhibits significantly higher conductivity than si-$MoSe_2$/$MoSe_2$, delivering a current of 1447 μA/μm at a bias of 0.7 V and a low contact resistance of 242 $\Omega\cdot\mu$m. Moreover, the heterojunction features a low contact-potential difference, which supports low-voltage operation. This design opens a new, all-2D material route toward advanced electronic devices at the sub-3 nm node.

Keywords: Self-intercalation; MoX_2; Transport; First principles

1. Introduction

As the scaling of integrated circuit technology approaches the nanoscale, silicon-based semiconductor devices are confronting fundamental physical limits, including pronounced short-channel effects and quantum tunneling[1-3]. In this context, two-dimensional (2D) semiconductors with atomic-layer thickness have emerged as promising candidates for sustaining Moore's Law, benefiting from their superior electrostatic gate control and high carrier mobility. Particularly, 2D transition metal dichalcogenides (TMDCs, MX_2) have garnered significant interest owing to their tunable bandgaps and favorable integration compatibility. Nevertheless, the excessively high contact resistance at the metal-semiconductor interface remains a critical bottleneck,

E-mail: redlxj@126.com (Xiaojie Liu),wh@fysik.cn (Hui Wang),wlyht@126.com (Haitao Yin)

impeding the harnessing of these intrinsic advantages for high-performance transistors. This issue primarily originates from two mechanisms: (i) a high Schottky barrier due to the misalignment between the metal work function and the semiconductor bands, and (ii) severe Fermi-level pinning (FLP) induced by metal-induced gap states (MIGS) or defect-induced gap states (DIGS) at the interface. Moreover, for atomically thin channels, the conventional use of three-dimensional metal electrodes often introduces lattice mismatch and interfacial defects, further aggravating performance degradation[4,5].

To address this challenge in 2D semiconductor contacts, various strategies have been explored. Two-dimensional layered metals have emerged as promising contact electrodes for suppressing FLP, enabling the fabrication of carrier-polarity-tunable field-effect transistors. However, the van der Waals gaps at the interface introduce an additional tunneling barrier that degrades carrier injection, keeping the contact resistance above the quantum limit. Semimetals are another candidate for electrode materials, leveraging their low density of states at the Fermi level (E_f) to suppress MIGS and enhance contact properties. Bismuth (Bi) and antimony (Sb) electrodes, for instance, have achieved contact resistances as low as 42 $\Omega\cdot\mu$m[6,7]. However, the selection of these semimetallic electrode materials is quite limited, and they are typically compatible with only specific 2D semiconductor systems[8], thus limiting their broad applicability.

Intercalation engineering provides a distinct and versatile route to tailor material properties at the atomic scale[9–11]. By inserting selected atoms into the van der Waals gaps of MX_2, precise control over its electronic[12,13], magnetic[14,15], and optoelectronic[16]properties can be achieved. For instance, intercalation of Li, Ca, or Fe into bilayer 2H-MoS_2 can induce superconductivity or ferromagnetism[17–19]. Crucially for contact engineering, intercalation enables in situ formation of high-quality metal-semiconductor junctions. Intercalation of Co/Cu into bilayer SnS_2 (Co/Cu-SnS_2) locally converts the semiconductor into a metallic phase[20]. Devices constructed with this metallic region as an electrode, such as Co-SnS_2/SnS_2 junctions, exhibit low contact resistances down to 30.1 $\Omega\cdot\mu$m[21]. Similarly, Cu-MoS_2/MoS_2 heterojunctions form low-resistance ohmic contacts with values approaching or even surpassing the quantum limit of ~30 $\Omega\cdot\mu$m[22]. A particularly promising extension is self-intercalation (si), which occurs under metal-rich conditions and transforms MX_2 into stable metallic si-MX_2 phases[23–25]. Through self-intercalation, metallic si-MX_2 electrodes can

be seamlessly patterned within a semiconducting MX_2 host, creating a lateral heterojunction that is chemically homogeneous and perfectly lattice-matched.

In this work, we employ the first-principles approach combining non-equilibrium Green's function (DFT-NEGF) method to investigate the electronic structure of si-MoX_2 (X = S, Se) and the quantum transport in si-MoX_2/MoX_2 lateral heterojunctions. Our calculations reveal relatively low Schottky barrier heights of 0.5 eV and 0.6 eV for si-MoS_2/MoS_2 and si-$MoSe_2$/$MoSe_2$, respectively. At low operating voltages, the si-MoS_2/MoS_2 device delivers a high on-state current (I_{on}) of 1262 μA/μm at a bias of 0.64 V, outperforming the si-$MoSe_2$/$MoSe_2$ counterpart. Moreover, the si-MoS_2/MoS_2 junction achieves a low contact resistance of 242 $\Omega\cdot\mu$m. This work moves beyond conventional heterojunction design paradigms and provides a novel theoretical strategy for developing high-performance tailored electronic devices.

2. Calculation methods

Geometric and electronic properties were computed using density functional theory (DFT) as implemented in the plane-wave code VASP. All calculations employed the Perdew–Burke–Ernzerhof (PBE) functional under the generalized gradient approximation (GGA) to describe exchange-correlation effects[26,27], with van der Waals interactions corrected by Grimme's DFT-D3 method[28]. The plane-wave cutoff energy was set to 500 eV, and convergence thresholds for atomic forces and total energy were set to 0.02 eV/Å and 1×10^{-5} eV/atom, respectively.

Electronic transport properties were investigated using NanoDCAL software package [29,30]. The exchange-correlation functional was chosen as GGA-PBE96. A double-zeta plus polarization (DZP) atomic-orbital basis set was adopted, and norm-conserving pseudopotentials were used to describe the interaction between nuclei and core electrons. The real space grid was set to 29 × 233 × 587. For the electrode and central scattering regions, k-point samplings of 19×1×100 and 19×1×1 were used, respectively. The transport direction (z-axis) was sampled with pa high density to ensure accurate density-of-states calculations.

3. Results and Discussion

Based on the atomic structure of bilayer MoX_2 (BL-MoX_2), we systematically investigated their self-intercalated configurations within both AA and AA′ stacking orders, as illustrated in Figs. 1(a)-(d). A vacuum spacing of 25 Å was implemented in the vertical direction to prevent artifacts

due to the interaction of periodic images. The self-intercalated structures, denoted as si-MoS_2 and si-$MoSe_2$, were constructed by inserting an additional Mo atom into the van der Waals gap of the bilayer. We then performed full atomic relaxation and lattice optimization for the unit cells of these configurations. The optimized structural parameters are summarized in Table 1. After relaxation, the lattice constant a of si-MoS_2 reduced from 3.19 Å (pristine bilayer) to 3.16 Å for both stacking configurations. In contrast, si-$MoSe_2$ exhibited no significant change in lattice parameter, with remaining at a = 3.33 Å. In the AA-stacked configuration (Figs. 1(a)-(b)), the intercalated Mo atom resides symmetrically between the two chalcogen (X) layers, resulting in equal vertical distances to the upper and lower X planes ($d_1 = d_2$). For the AA′ stacking (Figs. 1(c)-(d)), the intercalant occupies a site directly beneath an upper-layer X atom and above a lower-layer Mo atom. The corresponding vertical distances are d_1 = 2.37 Å (si-MoS_2) and 2.49 Å (si-$MoSe_2$) to the upper X layer, and d_2 = 1.45 Å (si-MoS_2) and 1.53 Å (si-$MoSe_2$) to the lower Mo layer.

Metal self-intercalation serves as an effective approach to modulate both the electronic structure and stability of MoX_2. Projected band structure analyses indicate that si-MoX_2 exhibits metallic behavior in both AA and AA′ stacking configurations. The unoccupied states of the intercalated Mo atom (Mo(si)) undergo strong hybridization with the conduction bands of the BL-MoX_2, thereby forming partially occupied hybrid states near the Fermi level. Concurrently, the overall band structure of BL-MoX_2 shifts downward, collectively contributing to the establishment of efficient conductive channels. This hybridization effect is especially pronounced in the AA′ stacking, which exhibits stronger orbital coupling and superior charge transport capability. Phonon spectrum calculations elucidate the distinct stability of the two configurations. The AA stacking displays an imaginary frequency mode near the Fermi level, reflecting its poor dynamical stability, while AA′ stacking shows no anharmonic vibrational modes, confirming its robust structural stability. Consequently, self-intercalated MoX_2 preferentially stabilizes in the AA′ stacking configuration, which integrates excellent metallic conductivity with high structural robustness. Subsequent investigations will therefore concentrate on this particular configuration.

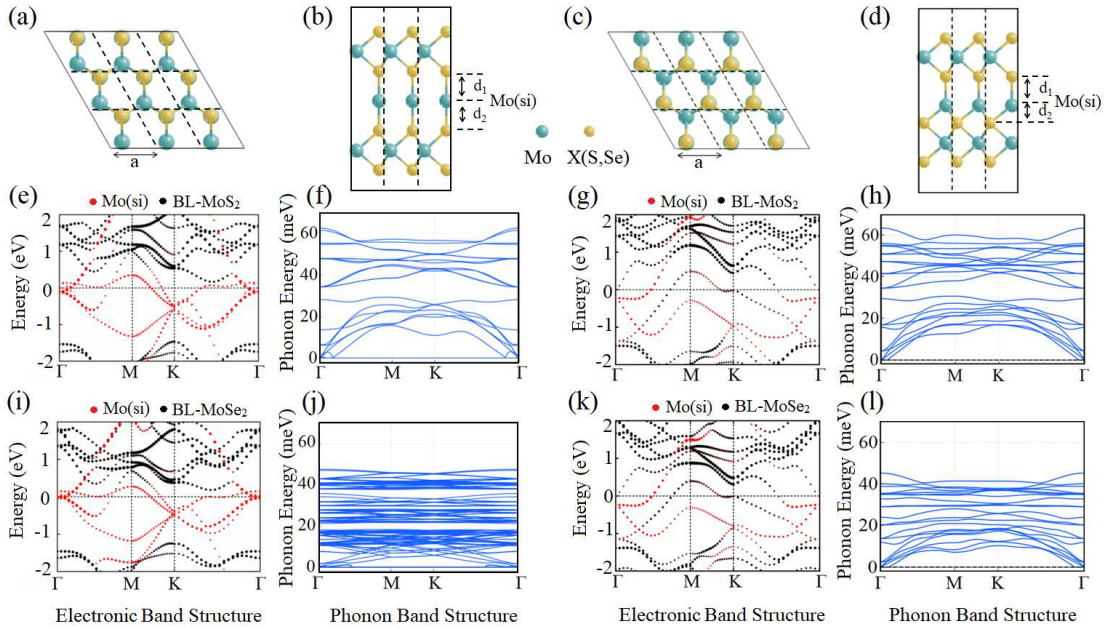

Fig. 1 Structural, electronic, and vibrational properties of si-MoX_2 in AA and AA' stacking configurations. (a) Top and (b) side views of the AA-stacked si-MoX_2 (3×3 supercell). (c) Top and (d) side views of the AA'-stacked si-MoX_2 (3×3 supercell). (e) Band structure and (f) phonon spectrum of AA-stacked si-MoS_2. (g) Band structure and (h) phonon spectrum of AA′-stacked si-MoS_2. (i) Band structure and (j) phonon spectrum of AA-stacked si-$MoSe_2$. (k) Band structure and (l) phonon spectrum of AA′-stacked si-$MoSe_2$.

Table 1 Lattice Parameters and Interatomic Distances for si-MoS_2 and si-$MoSe_2$ in AA and AA' Stacking Configurations

	MoS_2	AA-MoS_2	AA'-MoS_2	$MoSe_2$	AA-$MoSe_2$	AA'-$MoSe_2$
a (Å)	3.19	3.16	3.16	3.33	3.33	3.33
d_1 (Å)	/	2.40	2.37	/	2.52	2.49
d_2 (Å)	/	2.40	1.45	/	2.52	1.53

The differential charge density distributions in Figs. 2(a) and (b) reveal pronounced electron sharing between Mo(si) and the adjacent S/Se atoms, confirming the formation of stable covalent bonds within the van der Waals gap. This covalent bonding induces substantial interfacial charge transfer. Bader charge analysis reveals a net electron transfer from the Mo(si) layer to the BL-MoX_2 substrate, with the values being significantly larger for si-MoS_2 (0.61 e) than for si-$MoSe_2$ (0.1 e). This interfacial charge redistribution is identified as the primary cause of the overall downward shift in the BL-MoX_2 band structure. Further density of states (DOS) analysis in Figs. 2(c) and (d) shows that the electronic states near the Fermi level are dominated by the BL-MoX_2 substrate, with its

contribution significantly exceeding that of the intercalated Mo(si). Such synergistic electronic reorganization, in which the host BL-MoX_2 matrix plays a dominant role and the Mo(si) acts as a modulator, constitutes the fundamental mechanism driving the metallization transition in this system.

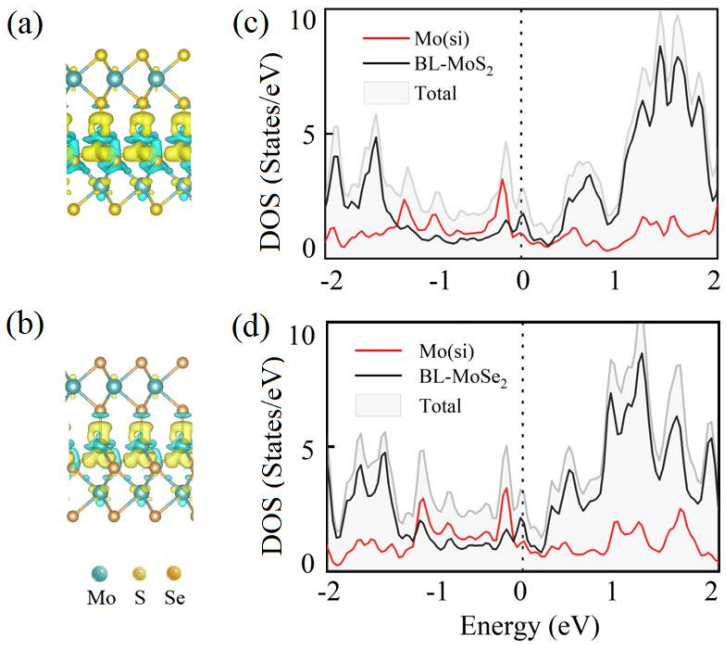

Fig. 2 Charge density differences for (a) si-MoS_2 and (b) si-$MoSe_2$ supercell along the z-direction. The yellow and cyan colors correspond to regions of charge accumulation and depletion. DOS of (c) si-MoS_2 and (d) si-$MoSe_2$ unit cell. The red and black lines indicate the contribution from the Mo(si) and the BL-MoS_2 or BL-$MoSe_2$, respectively.

To investigate the electronic transport properties, a full MoX_2-based field-effect transistor was constructed along the armchair (AC) direction, as illustrated in Fig. 3. The central scattering region consists of intrinsic semiconducting MoX_2 with four unit cells, yielding lengths of approximately 21 Å for MoS_2 and 23 Å for $MoSe_2$. The left and right electrodes are formed by metallic si-MoX_2, which extends periodically along the transport direction (z-axis) to model semi-infinite leads. Enabled by the self-intercalation technique, a lattice-matched seamless edge contact is achieved at the electrode-center interface. To prevent spurious interlayer coupling, a vacuum layer of 25 Å was applied along the non-periodic (y) direction. All atomic structures at the junction were fully relaxed and optimized using the VASP package.

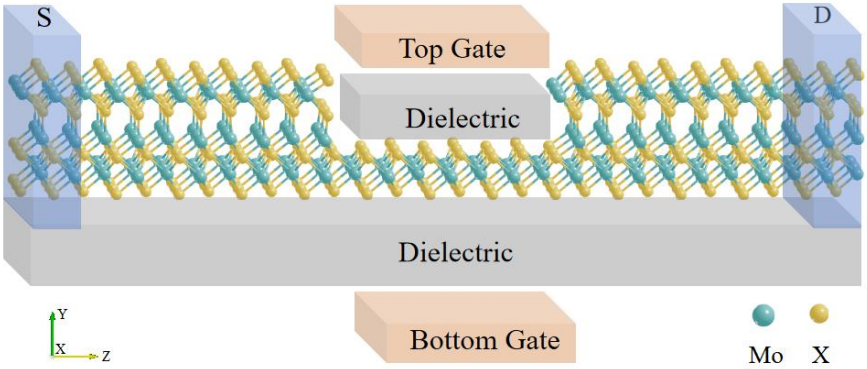

Fig. 3 Schematic illustration of the si-MoX_2/MoX_2/si-MoX_2 field-effect transistor along the AC direction. S and D denote the source and drain electrodes, respectively.

To characterize the electrical contact properties of the si-MoX_2/MoX_2 interface, the projected local density of states (PLDOS) at equilibrium was computed by projecting the total density of states onto atomic orbitals and arranging it along the transport direction. This analysis offers a detailed view of the electronic structure at the metallic-semiconductor interface. As shown in the left panels of Figs. 4(a) and (b), the PLDOS of the metallic si-MoX_2 buffer layer and the semiconducting MoX_2 central region illustrates the contact characteristics and band alignment for the si-MoS_2/MoS_2 and si-$MoSe_2$/$MoSe_2$ junctions, respectively. In Fig. 4(a), the dark blue region between 21-41 Å reflects the low-DOS band gap of MoS_2, whereas the corresponding 23-46 Å region in Fig. 4(b) corresponds to the band gap of $MoSe_2$. The energy difference between the E_f and the conduction band minimum (CBM), corresponding to the Schottky barrier height Φ_{SB}, is calculated to be 0.50 eV for the si-MoS_2/MoS_2 contact (Fig. 4(a)). For si-$MoSe_2$/$MoSe_2$, the barrier height is 0.60 eV, slightly higher than that of the MoS_2-based junction (Fig. 4(b)). Notably, both values are lower than the 0.8 eV barrier reported for phase-engineered MoS_2 heterojunctions[31]. Such a reduced barrier favors low-energy electron injection and supports measurable current flow even under small bias voltages. Additionally, a distinct high-DOS region is visible at the metal-semiconductor interface, as indicated by the black dashed boxes in the figures. This feature stems from interface states associated with the metallic material, which can be further examined through the local density of states (LDOS) profiles at E = 0 eV under equilibrium conditions (Figs. 4(c)-(d)). Specifically, the metallic edge exhibits a pronounced density of states, while the semiconductor layer in direct contact also contributes a moderate DOS, resulting in a localized high-DOS zone at the interface.

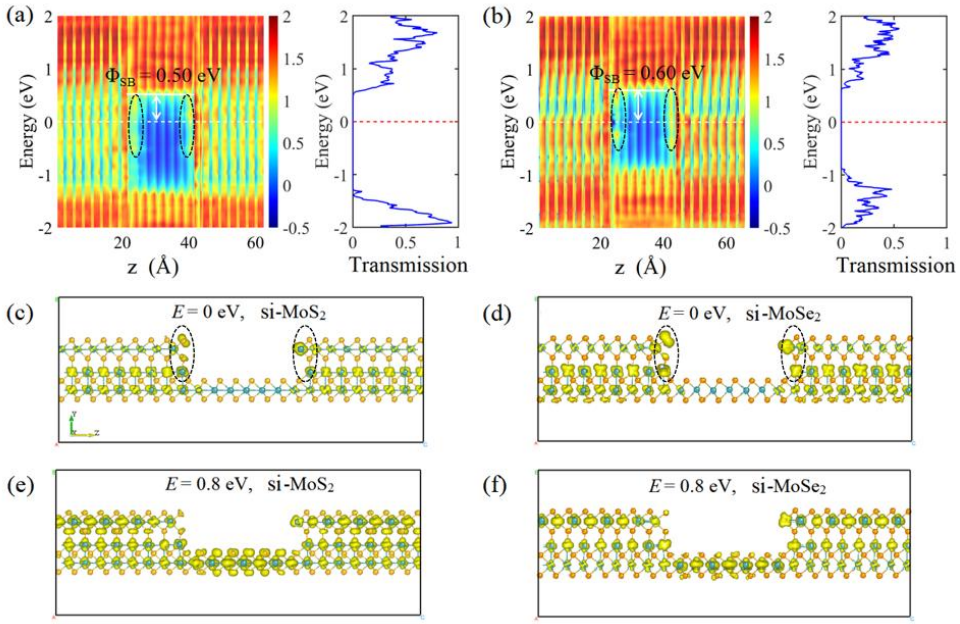

Fig. 4 PLDOS, transmission coefficient, and LDOS for the si-MoX_2/MoX_2/si-MoX_2 devices. PLDOS (plotted on a logarithmic scale) and transmission at equilibrium for the (a) MoS_2-based and (b) $MoSe_2$-based devices. The white (red) dashed and solid lines indicate the E_f and the CBM of the central MoX_2 region, respectively. The white arrow marks the Schottky barrier height (Φ_{SB}). LDOS at E = 0 eV for the (c) MoS_2-based and (d) $MoSe_2$-based devices. Corresponding LDOS at E = 0.8 eV for the (e) MoS_2-based and (f) $MoSe_2$-based devices.

The Schottky barrier height critically determines the electron transport characteristics of MoX_2 under non-equilibrium conditions. The transmission spectra, presented in the right panels of Figs. 4(a) and (b), show no significant peaks near the Fermi level. This absence confirms that the intrinsic bandgap of MoX_2 effectively blocks low-energy electron tunneling. At higher energies, distinct peak features emerge, indicating the opening of efficient tunneling channels. A direct comparison between the two systems reveals that the overall transmission coefficients are consistently higher for MoS_2 than for $MoSe_2$. This disparity is closely linked to their differing PLDOS profiles. To identify the microscopic origin of this difference, we examined the LDOS at an energy of 0.8 eV. As shown in Figs. 4(e) and (f), the LDOS within the central scattering region is substantially greater for MoS_2 than for $MoSe_2$. This higher LDOS signifies a larger number of electronic states available for tunneling in MoS_2 at this energy, which directly accounts for its correspondingly higher transmission coefficient along the transport direction.

The tunneling barrier serves as a pivotal parameter in determining the performance of

semiconductor-metal contacts and can be directly assessed through the effective potential (V_{eff}). We calculated the V_{eff} across the si-MoX_2/MoX_2 interface, as shown in Fig. 5. The tunnel barrier height Φ_{TB} is defined as the minimum energy barrier for electrons crossing from the Fermi level of metallic si-MoX_2 to that of semiconducting MoX_2 [32]. This quantity is obtained from the difference in V_{eff} between the gap (Φ_{gap}) and the MoX_2 region(Φ_{MoX_2}). The atomically seamless edge contact, which has negligible interfacial separation, allows Φ_{MoX_2} to exceed Φ_{gap}, thereby completely suppressing the tunneling barrier in all devices. This highlights a key structural advantage of the edge-contact geometry. Consequently, the si-MoX_2/MoX_2 interface achieves exceptionally high carrier injection efficiency, laying a robust foundation for realizing low contact resistance.

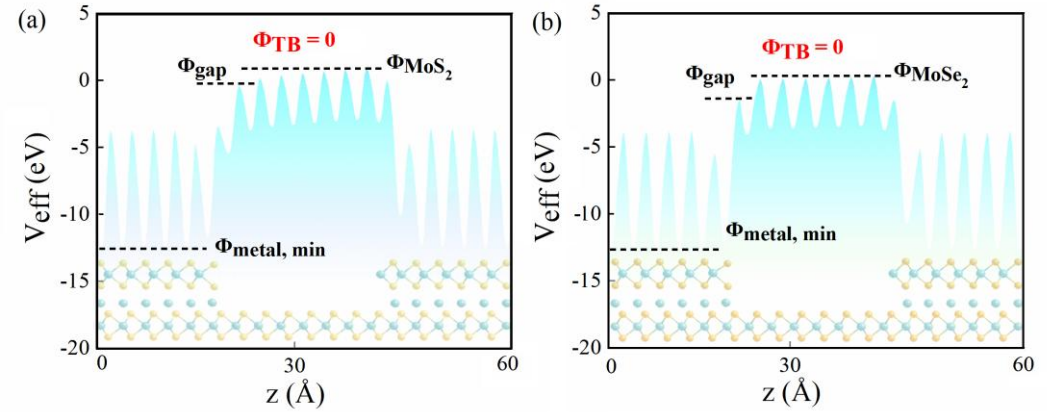

Fig. 5 Effective potential profile of the si-MoX_2/MoX_2/si-MoX_2 devices. (a)MoS_2-based device. (b) $MoSe_2$-based device. Here, Φ_{TB} denotes the effective tunnel barrier height, and $\Phi_{metal,\ min}$ indicates the minimum value of the effective potential (V_{eff}) within the metal electrode region.

Fig. 6(a) presents the *I-V* characteristics of the si-MoX_2/MoX_2/si-MoX_2 devices under varying source-drain voltage (V_{ds}). The non-linear increase in current with V_{ds} reveals distinct charge transport regimes at different biases. A comparison between MoS_2 and $MoSe_2$ channels shows a markedly superior current response in MoS_2. For instance, at 0.7 V, the MoS_2 device delivers 1447 μA/μm, nearly an order of magnitude higher than the 179 μA/μm for $MoSe_2$. With a channel length much shorter than the electron mean free path, transport is ballistic, making the total on-state resistance (R_{on}) dominated by contact resistance (R_C). The contact resistance was extracted from the *I-V* curves using $R_C = V_{ds}/2I$. The extracted R_C values, plotted versus V_{ds} in Fig. 6(b), decrease consistently with increasing bias. At V_{ds} = 0.7 V, the MoS_2 device achieves an R_C of 242 $\Omega\cdot\mu$m. This value is not only significantly lower than those of phase-engineered 1T/2H-MoS_2 heterojunctions

(30~40 kΩ·μm)[33]and Li-intercalated contacts (420 Ω·μm)[34], but also comparable to leading-edge results from semi-metallic Bi/MoS_2 (123 Ω·μm)[6] and Y-doped Y-MoS_2/MoS_2 junctions (117 Ω·μm)[35]. The performance clearly demonstrates the effectiveness of the self-intercalation method in forming low-resistance contacts.

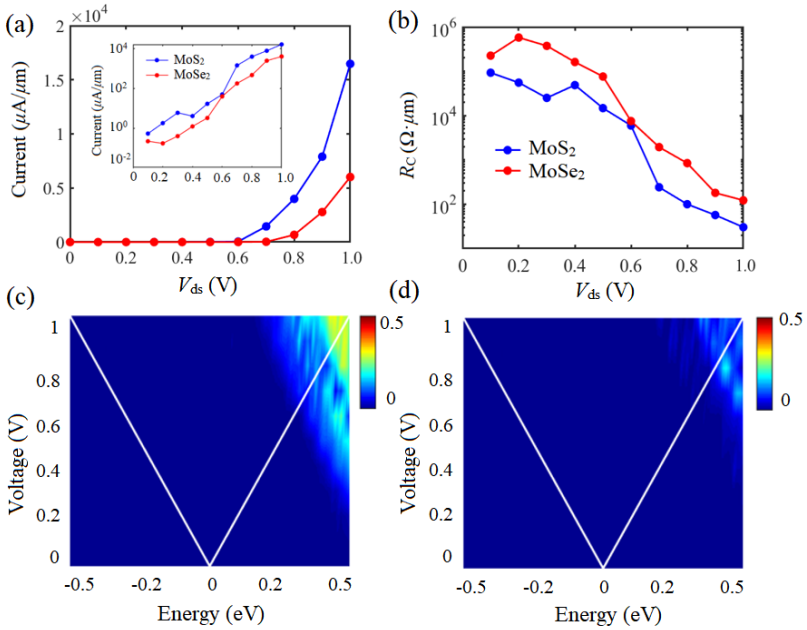

Fig. 6 Electrical transport characteristics of the si-MoX_2/MoX_2/si-MoX_2 devices. (a) *I-V* curves and (b) R_C versus bias voltage. Transmission spectra for the (c) MoS_2-based and (d) $MoSe_2$-based devices at different bias voltages. The white solid lines represent bias windows.

To further understand the current characteristics, we analyze the electron transmission spectra under non-equilibrium conditions. The current through the device is given by $I(V)=\frac{2e}{h}\int_{\mu_L}^{\mu_R}T(E,V)\left[f_L(E,\mu_L)-f_R(E,\mu_R)\right]\mathrm{d}E$, where *T(E,V)* is the energy and bias dependent transmission coefficient, $f_L(f_R)$ is the Fermi–Dirac distribution of the left (right) electrode, and the chemical potentials satisfy $\mu_L(\mu_R)$. Figs. 6(c) and (d) show the transmission spectra *T(E,V)* of the si-MoX_2/MoX_2/si-MoX_2 devices under biases from 0 to 1.0 V, with the bias window indicated by solid white lines. At V_{ds} < 0.7 V for MoS_2 and V_{ds} < 0.8 V for $MoSe_2$, the bias window contains no pronounced transmission peaks, consistent with the low observed current. As the bias increases further, transmission peaks corresponding to higher-energy states near the conduction band edge enter the window, leading to a sharp rise in current. A direct comparison reveals that the transmission peak amplitudes in the MoS_2 device (Fig. 6(c)) are consistently higher than those in the

$MoSe_2$ device (Fig. 6(d)) at the same bias, directly explaining the larger current in the MoS_2-based junction under identical operating conditions.

To examine the gate-tunable electrical behavior in two-dimensional semiconductor devices, a vertical electric field was applied to both MoS_2 and $MoSe_2$ devices (Fig. 2). Fig. 7 displays their transfer characteristics at a fixed drain-source voltage of V_{ds} = 0.64 V. The current increases with positive gate voltage (V_{gs}) and decreases under negative V_{gs}, confirming typical n-type conduction. The MoS_2 device exhibits an on-state current I_{on} of 1262 μA/μm at V_{gs} = 5 V, while the $MoSe_2$ device reaches 901 μA/μm at V_{gs} =10 V. Both values meet the high-performance benchmark (900 μA/μm) set by the International Technology Roadmap for Semiconductors (ITRS).

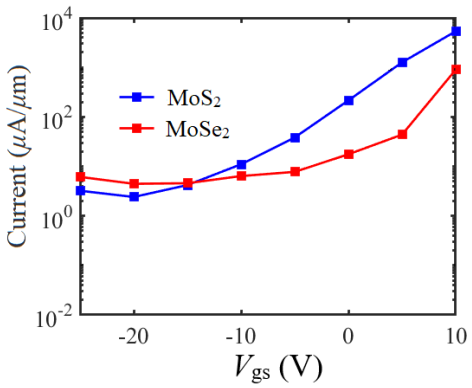

Fig. 7 Transfer characteristics of si-MoX_2/MoX_2/si-MoX_2 devices at V_{ds} = 0.64 V.

To elucidate the gate-tuning mechanism, the PLDOS and the transmission coefficients for MoS_2 and $MoSe_2$ channels at gate voltages of V_{gs} = -10 V, 0 V, and 10 V were calculated to analyzing the resultant band bending and conduction under combined gate and drain biases. As shown in Figs. 8(b) and (e), at V_{gs} = 0 V, the CBM of MoS_2 lies partially within the bias window, creating limited conduction channels. A corresponding pronounced transmission peak yields a current of 214 μA/μm. For $MoSe_2$, its higher CBM results in fewer available states within the bias window, leading to a lower current of only 17 μA/μm. Applying a positive gate voltage (V_{gs} = 10 V) induces electrostatic doping, which shifts the energy bands of the channel downward, as shown in Figs. 8(c) and (f). This brings more of the CBM into the bias window, significantly increasing the number of effective transmission channels. Concurrent band bending thins the potential barrier, making quantum tunneling the dominant transport mechanism and drastically enhancing the current. In this regime, the impact of the Schottky barrier height is diminished; the higher density of states in MoS_2 grants it a larger transmission coefficient and thus a higher current than $MoSe_2$. Conversely, under a negative

gate voltage V_{gs} = -10 V, the channel bands bend upward in Figs. 8(a) and (d), shifting the CBM outside the bias window. Thermionic emission then becomes the primary transport mechanism, rendering the current highly sensitive to the contact barrier height. Owing to its lower Schottky barrier, MoS_2 exhibits higher thermionic excitation efficiency, which results in a larger transmission coefficient and higher current under the same bias.

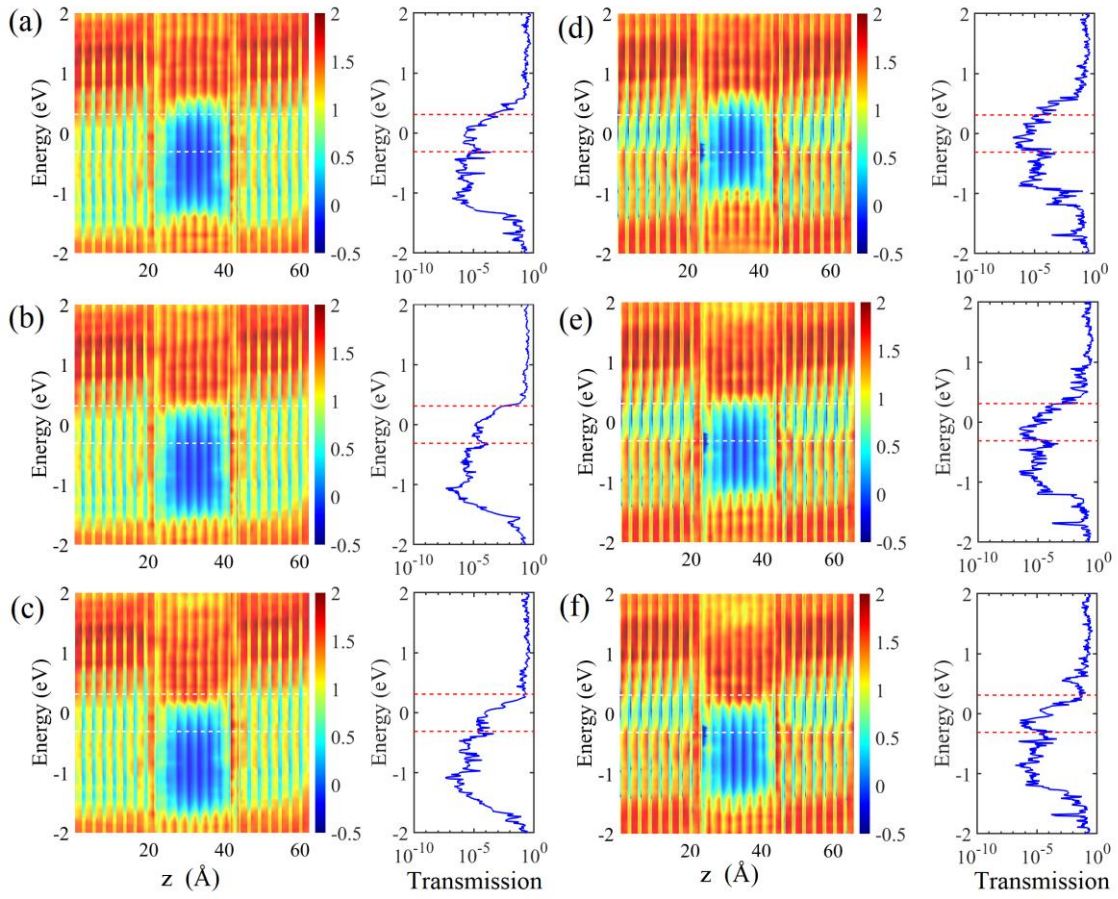

Fig. 8 PLDOS and Transmission coefficients on log y scale at different gate voltages at V_{ds} = 0.64 V. (a) V_{gs} = -10 V, (b)V_{gs} = 0 V and (c) V_{gs} = 10 V for MoS_2-based device; (d) V_{gs} = -10 V, (e) V_{gs} = 0 V and (f) V_{gs} = 10 V for $MoSe_2$-based device. The white and red dashed lines denote the bias window.

4. Conclusion

In this work, we systematically investigated the formation mechanism of metallic self-intercalated si-MoX_2 (X = S, Se) and the electronic transport properties of lateral heterojunctions formed between si-MoX_2 and semiconducting MoX_2 using DFT-NEGF method. The results demonstrate that the self-intercalation strategy enables the realization of an atomically smooth metal-semiconductor interface within the same MoX_2 material system. Its key advantage lies in the complete elimination of chemical heterogeneity and lattice mismatch inherent to conventional

heterostructures, thereby significantly suppressing interface defect formation. Our calculations reveal that the si-MoX_2/MoX_2 heterojunctions exhibit relatively low Schottky barrier heights (0.5 eV for si-MoS_2/MoS_2 and 0.6 eV for si-$MoSe_2$/$MoSe_2$). Moreover, the covalently bonded seamless connection essentially removes the tunneling barrier, enabling highly efficient carrier injection. The si-MoS_2/MoS_2 heterojunction-based field-effect transistor shows outstanding transport performance, achieving a current density of 1447 μA/μm and a low contact resistance of 242 $\Omega\cdot\mu$m, along with excellent gate-voltage modulation capability. This self-intercalation approach successfully realizes lateral heterojunctions that combine a low-damage interface with low contact resistance, offering a novel material system and device architecture solution for the development of high-performance two-dimensional electronic devices.

Data availability

The data supporting the findings of this paper are available from the corresponding authors upon reasonable request.

References

[1] Akinwande, D. et al. Graphene and two-dimensional materials for silicon technology. *Nature* 573, 507–518 (2019).

[2] Zheng, Y., Gao, J., Han, C. & Chen, W. Ohmic Contact Engineering for Two-Dimensional Materials. *Cell Reports Physical Science* 2, 100298 (2021).

[3] Wang, Y. & Chhowalla, M. Making clean electrical contacts on 2D transition metal dichalcogenides. *Nat Rev Phys* 4, 101–112 (2021).

[4] Kwon, G. et al. Interaction- and defect-free van der Waals contacts between metals and two-dimensional semiconductors. *Nat Electron* 5, 241–247 (2022).

[5] Batool, S., Idrees, M., Han, S., Roy, V. A. L. & Zhou, Y. Electrical Contacts With 2D Materials: Current Developments and Future Prospects. *Small* 19, 2206550 (2023).

[6] Li, W. et al. Approaching the quantum limit in two-dimensional semiconductor contacts. *Nature* 613, 274–279 (2023).

[7] Shen, P.-C. et al. Ultralow contact resistance between semimetal and monolayer semiconductors. *Nature* 593, 211–217 (2021).

[8] Lee, S. et al. Semi-Metal Edge Contact for Barrier-Free Carrier Transport in MoS_2 Field Effect Transistors. *ACS Appl. Electron. Mater.* 6, 4149–4158 (2024).

[9] Zhou, J. et al. Layered Intercalation Materials. *Advanced Materials* 33, 2004557 (2021).

[10] Xie, L. S., Husremović, S., Gonzalez, O., Craig, I. M. & Bediako, D. K. Structure and Magnetism of Iron- and Chromium-Intercalated Niobium and Tantalum Disulfides. *J. Am. Chem. Soc.* 144, 9525–9542 (2022).

[11] Zhou, T., Zhou, D., Wang, Y., Du, J. & Huang, Y. First-principles investigation on the interlayer doping of $SnSe_2$ bilayer. *J Nanopart Res* 20, 301 (2018).

[12] Tang, B. et al. Phase engineering of Cr_5Te_8 with colossal anomalous Hall effect. *Nat Electron* 5, 224–232 (2022).

[13] Huan, Y. et al. Composition-Controllable Syntheses and Property Modulations from 2D Ferromagnetic Fe_5Se_8 to Metallic Fe_3Se_4 Nanosheets. *Advanced Materials* 35, 2207276 (2023).

[14] Cui, F. et al. Epitaxial Growth of Step-Like Cr_2S_3 Lateral Homojunctions Towards Versatile Conduction Polarities and Enhanced Transistor Performances. *Small* 18, 2105744 (2022).

[15] Li, Z. et al. Intercalation Strategy in 2D Materials for Electronics and Optoelectronics. *Small Methods* 5, 2100567 (2021).

[16] Yang, W. et al. Tin Intercalated Ultrathin MoO_3 Nanoribbons for Advanced Lithium–Sulfur Batteries. *Advanced Energy Materials* 9, 1803137 (2019).

[17] Huang, G. Q., Xing, Z. W. & Xing, D. Y. Dynamical stability and superconductivity of Li-intercalated bilayer MoS_2 : A first-principles prediction. *Phys. Rev. B* 93, 104511 (2016).

[18] Szczōśniak, R., Durajski, A. P. & Jarosik, M. W. Metallization and superconductivity in Ca-intercalated bilayer MoS_2. *Journal of Physics and Chemistry of Solids* 111, 254–257 (2017).

[19] Kitaoka, Y., Ueda, A. & Imamura, H. Magnetism of MoS_2 bilayers with intercalated and surface adsorbed Fe. *Journal of Magnetism and Magnetic Materials* 594, 171895 (2024).

[20] Gong, Y. et al. Spatially controlled doping of two-dimensional SnS_2 through intercalation for electronics. *Nature Nanotech* 13, 294–299 (2018).

[21] Liu, M. et al. Anisotropic Low Schottky Barrier and Transport Properties of the Co-Intercalated Bilayer SnS_2/Monolayer SnS_2 Junction from First Principles. *ACS Appl. Electron. Mater.* 5, 2115–2121 (2023).

[22] Wang, H., Liu, X., Wang, H., Wang, Y. & Yin, H. Achieving Ultra-Low Contact Resistance via Copper-Intercalated Bilayer MoS_2. *Adv Elect Materials* 2500100 (2025).

[23] Zhao, X. et al. Engineering covalently bonded 2D layered materials by self-intercalation. *Nature* 581, 171–177 (2020).

[24] Han, Z. et al. Phase and Composition Engineering of Self-Intercalated 2D Metallic Tantalum Sulfide for Second-Harmonic Generation. *ACS Nano* 18, 6256–6265 (2024).

[25] Americo, S., Pakdel, S. & Thygesen, K. S. Enhancing Metallicity and Basal Plane Reactivity of 2D Materials via Self-Intercalation. *ACS Nano* 18, 4746–4755 (2024).

[26] Kresse, G., Furthmüller, J. & Hafner, J. Theory of the crystal structures of selenium and tellurium: The effect of generalized-gradient corrections to the local-density approximation. *Phys. Rev. B* 50, 13181–13185 (1994).

[27] Perdew, J. P., Burke, K. & Ernzerhof, M. Generalized Gradient Approximation Made Simple. *Phys. Rev. Lett.* 77, 3865–3868 (1996).

[28] Grimme, S., Antony, J., Ehrlich, S. & Krieg, H. A consistent and accurate ab initio parametrization of density functional dispersion correction (DFT-D) for the 94 elements H-Pu. *The Journal of Chemical Physics* 132, 154104 (2010).

[29] Taylor, J., Guo, H. & Wang, J. Ab initio modeling of quantum transport properties of molecular electronic devices. *Phys. Rev. B* 63, 245407 (2001).

[30] Kresse, G. & Joubert, D. From ultrasoft pseudopotentials to the projector augmented-wave method. *Phys. Rev. B* 59, 1758–1775 (1999).

[31] Kappera, R. et al. Phase-engineered low-resistance contacts for ultrathin MoS_2 transistors. *Nature Mater* 13, 1128–1134 (2014).

[32] Kang, J., Liu, W., Sarkar, D., Jena, D. & Banerjee, K. Computational Study of Metal Contacts to Monolayer Transition-Metal Dichalcogenide Semiconductors. *Phys. Rev. X* 4, 031005 (2014).

[33] Houssa, M., Meng, R., Afanas'ev, V. & Stesmans, A. First-Principles Study of the Contact Resistance at 2D Metal/2D Semiconductor Heterojunctions. *Applied Sciences* 10, 2731 (2020).

[34] Li, S. et al. Stabilizing Lithium Intercalation in MoS_2 for 2H-to-1T Phase Transition and Low-Resistance Edge Contacts. *Adv Materials Technologies* e01595 (2025).

[35] Jiang, J. et al. Yttrium-doping-induced metallization of molybdenum disulfide for ohmic contacts in two-dimensional transistors. *Nat Electron* 7, 545–556 (2024).

Acknowledgments

This research was supported by the Foundation of Heilongjiang Province Natural Science (grant no. PL2024A003), and the Youth Innovative Talent Project of the Basic Scientific Research Operating Expenses of Provincial Undergraduate Universities in Heilongjiang Province (grant no. 145209215). Haitao Yin thanks Li Niu for VASP calculation.

Author information

Authors and Affiliations

Key Laboratory for Photonic and Electronic Bandgap Materials of Ministry of Education, School of Physics and Electronic Engineering, Harbin Normal University, Harbin, 150025, China

Huan Wang, Xiaojie Liu, Hui Wang & Haitao Yin

College of Science, Qiqihar University, Qiqihar, 161006, China

Huan Wang

Contributions

X.J.L. and H.W. designed the research. H.T.T. and H.W. conducted the first-principles calculations and drafted the manuscript. All authors discussed the results and reviewed the manuscript. H.T.T. supervised the project.

Corresponding authors

Correspondence to Xiaojie Liu, Hui Wang or Haitao Yin.

Ethics declarations

Competing interests

The authors declare no competing interests.